Archives of Civil and Mechanical Engineering (2022) 22:146
https://doi.org/10.1007/s43452-022-00467-9

ORIGINAL ARTICLE

Material dynamic behavior in cutting zone of Inconel 718 and its influence on cutting process

Zhaopeng Hao[1] · Gang Cheng[1] · JiNing Li[3] · Yihang Fan[1,2]

Received: 8 February 2022 / Revised: 2 April 2022 / Accepted: 16 May 2022 / Published online: 13 June 2022

Abstract
The nickel-based superalloy Inconel 718 is widely used in aerospace and other fields due to its excellent performance. However, the alloy elements are presented in the form of compounds with high hardness, such as TiC, NbC, MoC, TiN and so on, which lead to complex cutting deformation in machining Inconel 718. In this study, the cutting experiments and the fast tool-drop test were carried out to obtain the chip root. Combining the split Hopkins pressure bar (SHPB) test, a scanning electron microscope (SEM) was used to observe the metallographic micrographs of the specimens and analyzed the plastic dynamic behavior of the material in the cutting area. The soft and hardening mechanism in the dynamic deformation process was described. The stress distribution model of material in the cutting area was proposed and the influence of stress distribution on cutting deformation, side flow and tool wear during the cutting process were also given.

Keywords Inconel 718 · Cutting deformation · Material dynamic behavior · Stress distribution · Tool wear

1 Introduction

Cutting mechanism is the mechanism of chip formation. In the cutting process, the deformation mechanism of the workpiece near the cutting edge is very important to explain the nature of the cutting phenomenon, which is the basis of cutting theory, including chip shape, cutting deformation process and its characteristics, formation of built-up-edge (BUE), etc. In high-speed cutting Inconel 718, the chip is serrated. The formation of the sawtooth chip has a great influence on the cutting force, surface quality fluctuation, and tool wear, which is the focus of theory and practice fields.

In the experiment of cutting Inconel718 with CBN tool by Costes et al. [2], it is observed that the chip has a shear localization phenomenon and forms a serrated chip. There are two main concentrated deformation areas, and the high pressure and high-temperature conditions in the cutting process change the microstructure. Su et al. [20] find out the correlation between the chip morphology at different sawtooth stages and the micro morphology of the machined surface in the high-speed cutting Inconel 718. In view of the formation mechanism of the serrated chip, the phenomenon of shear localization was observed in the cutting experiment of nickel-based superalloy Inconel 718 by Komanduri et al. [9] and it was considered that the formation mechanism of the serrated chip was similar to that of titanium alloy and high strength steel, mainly due to adiabatic shear. Similarly, in the experiments of cutting titanium alloy and AISI 52,100 by Recht [18, 19] and Dvaies [3, 4], the mechanism of the serrated chip is considered to be the effect of adiabatic shear, and the thermal softening of the material is better than the hardening effect.

Another point of view is that the cracks initiation on the free surface in cutting Inconel 718 led to serrated chip formation. Wang and Liu [26] used an orthogonal cutting Inconel 718 experiment to observe the chip morphology at different cutting speeds. It is found that dimples and ductile fracture exist on the free surface of serrated chip, and the fracture phenomenon is caused by adiabatic shear and severe plastic deformation. Obikawa et al. [17] analyzed

✉ JiNing Li
1026622048@qq.com

✉ Yihang Fan
fyh1911@126.com

[1] School of Mechatronic Engineering, ChangChun University of Technology, ChangChun 130012, China

[2] Key Laboratory of Advanced Manufacturing and Intelligent Technology (Ministry of Education), Harbin 150080, China

[3] Harbin Institute of Technology, Harbin 150001, Heilongjiang, China

Table 1 Chemical composition of IN718

Workpiece	Chemical composition									
	Ni	Cr	Nb	Mo	Ti	C	Si	Mn	B	Fe
Inconel 718	51.75	17	5.15	2.93	1.07	0.042	0.21	0.03	0.006	Other

Table 2 Physical and mechanical properties of IN718

Workpiece	Density, ρ (kg/m^3)	Yield strength, $\sigma_{0.2}$ (MPa)	Tensile strength, σ_b (MPa)	Elongation, δ_5 (%)	Shrinkage ratio, ψ (%)	Impact toughness, a_k (J/cm^2)
Inconel 718	8280	1260	1430	24	40	40

the formation mechanism of the sawtooth chip using the finite element analysis method, adopted the brittle fracture criterion of stress and strain rate as the boundary treatment, and considered that pressure and temperature were the main reasons for cracks in cutting deformation. When cutting high strength steel, Elbestawi et al. [5] and Shaw and Elbestawi [21] also came to a similar conclusion, believing that the formation mechanism of the serrated chip is the formation of micro-cracks on the free surface of the cutting layer and extending to the tool along the shear zone. In addition, chip morphology is affected by many factors, such as cutting tool vibration [22], cutting tool chip form Jawahir and Luttervelt [8], cutting zone temperature, application of cutting fluid, tool coating [29], cutting process parameters [10]. The texture of the material [11], all of these factors affect the chip formation in Inconel 718.

Based on the above analysis, the soft and hardening dynamic behavior of the material in the cutting zone is the key to the formation of the serrated chip during cutting Inconel 718. However, there is no clear description of the dynamic behavior of the material in the cutting zone in the literature. The research on the thermal softening behavior of Inconel 718 is mainly focused on high-temperature compression test. Thomas et al. [25] carried out the compression experiment of Inconel 718 at high temperature and low strain rate and established a hyperbolic sine constitutive model to describe the softening behavior of Inconel 718 material. Lin et al. [13] analyzed the influence of thermal deformation parameters (deformation temperature and strain rate) on flow stress by compression experiment and established a constitutive equation which can accurately reflect the thermal deformation behavior of nickel-based superalloy. Mahalle et al. [16] established a constitutive equation which can predict the flow stress of Inconel 718 under the condition of high temperature and low strain rate by means of a hot tensile test, and found the dynamic recrystallization phenomenon of the material at high temperature by using EBSD analysis. Through Inconel 718 static tensile test, Socha et al. [23] concluded that the surface crack was related to plastic deformation, and pointed out that hard phase point and grain boundary contributed to crack initiation.

Table 3 Physical and mechanical properties of tool

Tool material	Density (kg/m^3)	Elastic model (MPa)	Poisson's ratio ν	Specific heat capacity (J/kg °C)	Temperature conductivity (W/m °C)
WC–Co (8/%)	14.6	6.4×10^5	0.22	220	75.4

In this paper, based on the high-speed cutting characteristics of Inconel 718, the plastic dynamic behavior of the material in the cutting area and the soft and hardening mechanism in the dynamic deformation process are studied through the cutting experiments, the fast tool-drop test and SHPB test.

2 Experimental process

The material used in the cutting experiment is Inconel 718, whose chemical composition and physical properties are shown in Tables 1 and 2.

The cutting tool is co WC cemented carbide. The rake angle of the cutting tool is 0° and the relief angle is 6°. The material properties of the tool are shown in Table 3

CA6140 ordinary lathe is selected as the cutting experimental machine tool, which can realize stepless speed change. Explosive fast tool-drop test is adopted in the cutting process. The quick stop device can make the tool leave the test piece quickly during the turning process, and "freeze" the cutting state at the instant of tool withdrawal, so as to obtain the chip root and retain the cutting state of high temperature and high strain rate in the cutting area. The dynamic removal process of materials can be analyzed through the metallographic of chip root.

The high-temperature compression split Hopkinson bar (SHPB) test was also carried out to study the dynamic behavior of Inconel 718 at high temperature and high strain

rate. When the bullet collides with the input rod, an incident wave is generated. Due to the difference in wave impedance, when the incident wave reaches the end face of the input rod and the specimen contact, transmission and reflection phenomena will occur. In addition to reflecting back to the input rod to form a reflected wave, another part of the pulse will form a transmitted wave, which will be transmitted to the test piece for impact loading, and then transmitted to the output rod, and finally captured by the absorption rod. The tested sample is placed between the input rod and the output rod and bears different strain rates and different temperatures. The experimental parameters are shown in Table 4.

The integrated experimental system is shown in Fig. 1.

Table 4 SHPB test parameters

T_t (°C)	Strain rates (s^{-1})			
20 °C (T_{room})	5000 s^{-1}	7000 s^{-1}	9000 s^{-1}	11,000 s^{-1}
500 °C, 600 °C	Specimen sizes (D×L)			
700 °C, 800 °C	Φ4×2(mm)			

3 Results and discussion

3.1 Morphology and microstructure of chip root

The micro morphology of chip root [7] was obtained in the previous study of the author, as shown in Fig. 2. The cutting speeds are 40 m/min, 80 m/min and 100 m/min, respectively. It can be found that the cutting deformation is uneven at different cutting speeds, and the chip shape is serrated. The formation process of serrated chip is the performance that the removed material evolves from a stable state to an unstable state in the process of high-speed cutting, and finally reaches a self-adaptive process of stable state. The cutting layer material produces elastic deformation under the extrusion of the tool.

Chip subjected the force on the tool rake face and led to the extrusion of the cutting layer so that the shear slip in the lower cutting layer near the tip of the area began to deformation. At this time, the shear slip was spiky. It grew inside the cutting layer and gradually extended to

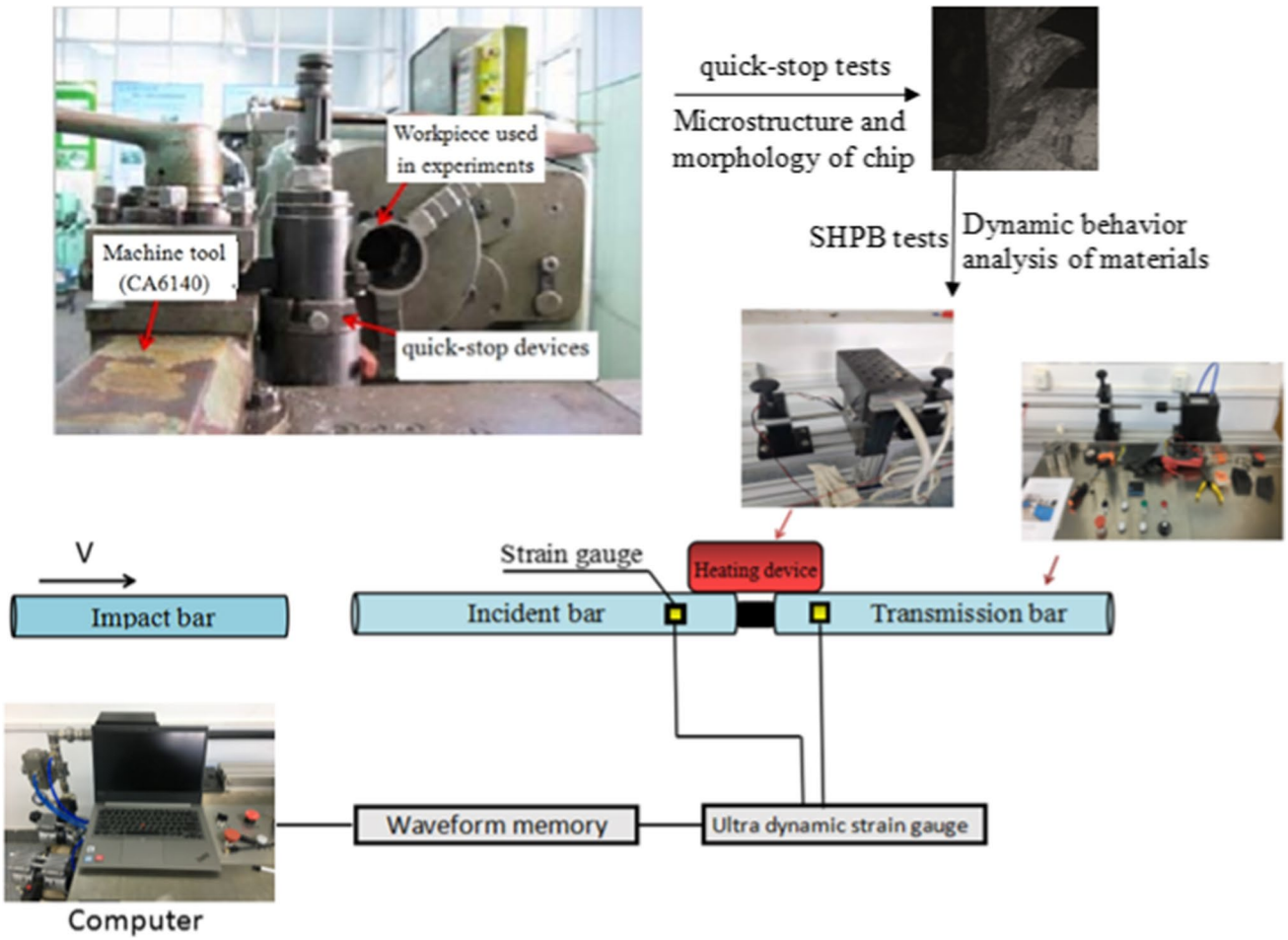

Fig. 1 Schematic diagram of the comprehensive experimental system

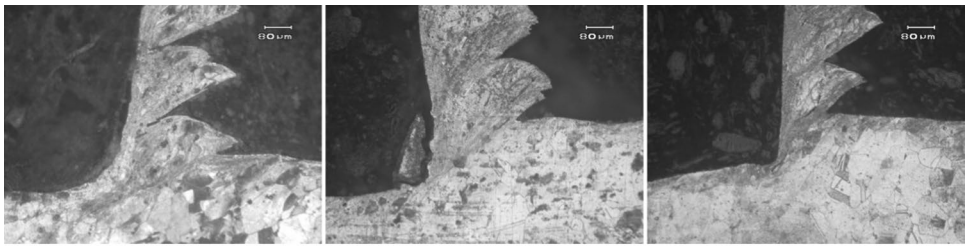

Fig. 2 Metallographic micrograph of chip root under different cutting conditions

(a) 40m/min **(b)** 80m/min **(c)** 100m/min

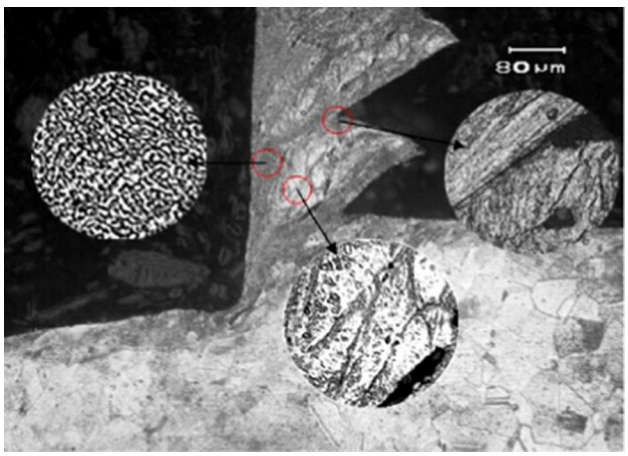

Fig. 3 Microstructure of chip root

the top surface of the cutting layer. The direction of shear force changed continuously to the cutting layer, and the shear slip instantly extended to the top surface of the cutting layer, forming a shear surface with a certain width. With the cutting process, the sawtooth chip formed under the action of shear force.

According to Fig. 2, shear localization and cracks can also be clearly observed. Serrated chip is a typical feature of chip morphology in high-speed cutting nickel-based superalloy Inconel 718.

It can be seen from Fig. 2 that during the sawtooth chip formation at a cutting speed of 100 m/min, severe deformation occurs between two blocks and at the bottom of the chip to form a banded structure and the grains in the band are refined. It is difficult to distinguish the slip line by optical microscope, and a transition band characterized by microstructure refinement appears. Fine grains can be observed in the transition zone, and dynamic soft behavior occurs. In the middle of each chip segment, the grain is slightly deformed and elongated, and the slip line can be clearly seen, and the hardening behavior of the material occurs. However, cracks appear on the free surface of the chip edge, and the overall microstructure of the chip is shown in Fig. 3.

3.2 Flow stress

The variation characteristics of flow stress can usually describe the hardening and softening behaviors during plastic working. It can be expressed as:

$$\theta = \partial\sigma/\partial\varepsilon. \tag{1}$$

In Eq. (1), θ is the hardening rate of the workpiece, σ is the stress and ε is the strain. At high temperature, the metal flow process can be divided into two stages. When $\theta > 0$, work hardening occurs, and when $\theta < 0$, dynamic softening occurs. The stress–strain curves at different strain rates and temperatures were obtained by SHPB experiment, as shown in Fig. 4.

According to Fig. 4, it can be found that the stress–strain curve after dynamic compression can be divided into two stages, which includes strain, strain rate hardening stage and temperature softening stage. The stress increases gradually, then the area is gentle, and finally the stress decreases with the increase of strain. In Fig. 4, the flow stress value at a given strain rate decreases significantly with the increase of temperature, indicating that the influence of temperature on Inconel 718 is highly sensitive. At a given temperature, the flow stress increases with the increase of strain rate. When it reaches 11,000 s^{-1}, the stress decreases, and it can be found that the change of stress value with strain rate is not obvious. It shows that the strain rate is less sensitive to Inconel 718 material. To observe the dynamic state of the material under different temperature and strain rate conditions, SHPB experiment was carried out and microscopic metallographic pictures at different strain rates and cutting temperatures are shown in Fig. 5.

It can be seen from Fig. 5 that dynamic recrystallization occurs in the process of high-temperature deformation to refine the microstructure, which is the main reason for softening behavior. At the same temperature, the increase in strain rate can inhibit the dynamic recrystallization phenomenon, and grain breakage occurs. At the same strain rate, with the increase in temperature, the dynamic recrystallization effect is obvious, and the dynamic recrystallization occurs preferentially at the deformed grain boundary.

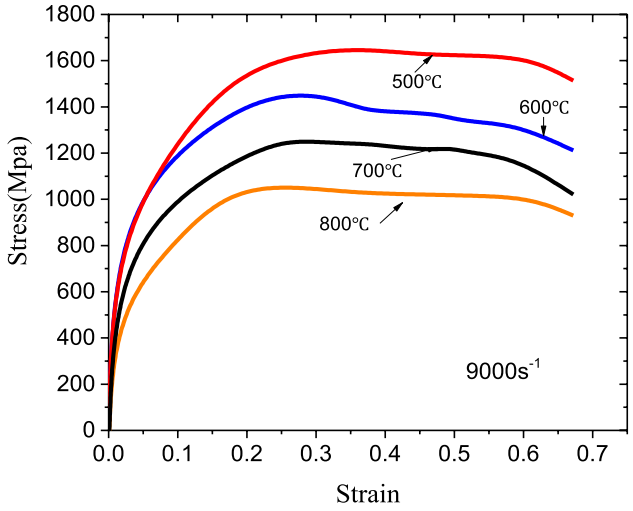

(a) Variation of flow stress with strain under different temperatures

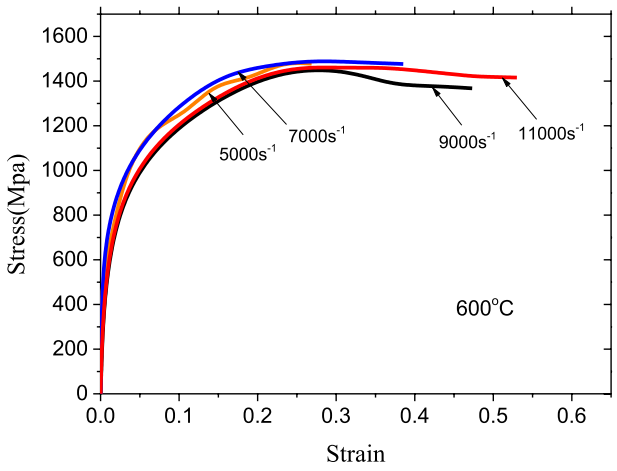

(b) Variation of flow stress with strain under different strain rates

Fig. 4 Flow stress curve

3.3 Description of material dynamic behavior in cutting zone

In the process of high-speed cutting Inconel 718, the deformation behavior of the alloy is very complex. The cutting process can be regarded as the dynamic compression process of material under high temperature and high strain rate. With the increase in cutting speed, the strain rate of material increases in the deformation process, and the phenomenon of work hardening and material softening occur simultaneously in the cutting area. Both work hardening and softening have a great influence on the cutting deformation behavior, especially on the serrated chip formation during high-speed cutting. Therefore, it is necessary to study the dynamic behavior of materials at high temperature and high strain rate. The grain size, temperature and strain rate are closely related to the flow stress in the process of material deformation, so it can be considered that the flow stress constitutive equation can reflect the material dynamic behavior evolution in the plastic deformation process.

3.3.1 Work hardening

According to the constitutive equation proposed by Cingara [1], the flow stress constitutive model of material during work hardening can be expressed as follows:

$$\frac{\sigma}{\sigma_p} = \left[\frac{\varepsilon}{\varepsilon_p}\exp\left(1-\frac{\varepsilon}{\varepsilon_p}\right)\right]^S. \tag{2}$$

where σ_p is the peak stress, ε_p is the peak strain, S is the material constant. In Eq. (2), the peak stress σ_p and peak strain ε_p can be calculated from the stress–strain curve obtained by SHPB tests.

Previous studies have shown that there is a process of thermal activation during high-temperature deformation. The Arrhenius, a hyperbolic sine function containing thermal activation, can better describe the relationship between strain rate and temperature [24], which is shown as Eq. (3).

$$\begin{cases} \dot{\varepsilon} = Af(\sigma_p)\exp(-Q_{act}/RT) \\ f(\sigma_p) = \left[\sinh(\xi\sigma_p)\right]^n. \end{cases} \tag{3}$$

There are two other models of Arrhenius type that are largely applied to explore the constitutive relationship [24]:

$$\dot{\varepsilon}=A_s\sigma_p^n\exp(-Q_{act}/RT)\ \xi\sigma_p < 0.8, \tag{4}$$

$$\dot{\varepsilon} = A_s\exp(\beta\sigma_p)\exp(-Q_{act}/RT)\ \xi\sigma_p > 1.2, \tag{5}$$

where A_s is constant, β and ξ stress adjustment factor which expressed by the following formula $\xi = \beta/n$.

Zener and Hollomon [27] proposed and verified the relationship between the strain rate $\dot{\varepsilon}$ and temperature T.

$$Z = \dot{\varepsilon}\exp\left(\frac{Q_{act}}{RT}\right) = A_n[\sinh(\xi\sigma_p)]^{n_0}. \tag{6}$$

Combined with Eqs. (3) and Eq. (6), the peak stress σ_p can be rewritten as Eq. (7).

$$\sigma_p = \frac{1}{\xi}\left\{\left(\frac{Z}{A_n}\right)^{1/n} + \left[\left(\frac{Z}{A_n}\right)^{2/n}+1\right]^{0.5}\right\}. \tag{7}$$

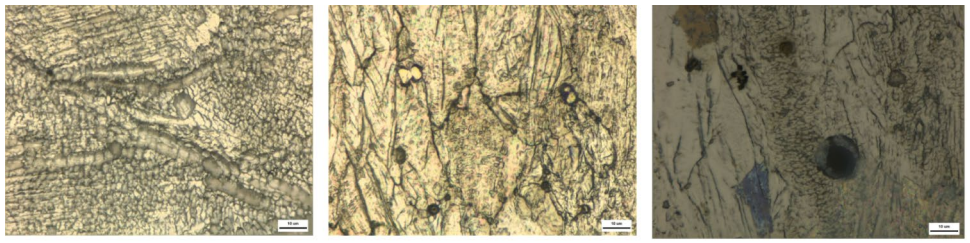

Fig. 5 Microscopic metallographic pictures at different strain rates and cutting temperatures

(a) Microscopic metallographic pictures at different strain rates（$\theta = 600^{o}$）

(b) Microscopic metallographic pictures at different cutting temperatures（$\dot{\varepsilon} = 7000s^{-1}$）

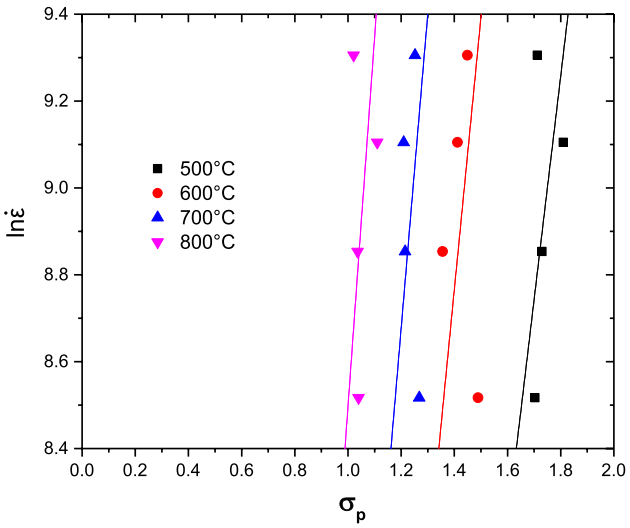

Fig. 6 $\ln\dot{\varepsilon} - \sigma_p$ curve

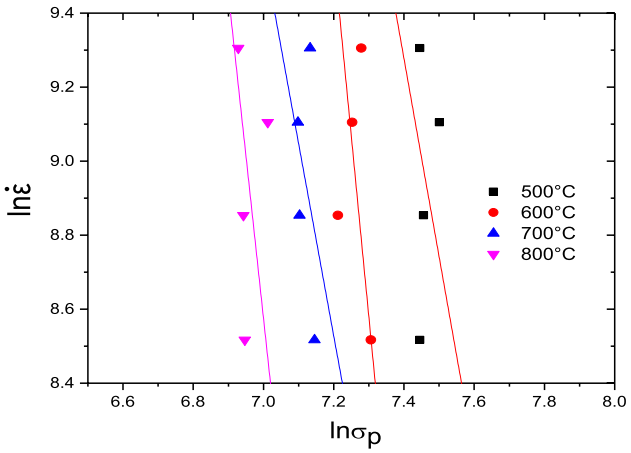

Fig. 7 $\ln\dot{\varepsilon} - \ln\sigma_p$ curve

Take logarithm on both sides of Eq. (7) to obtain:

$$\ln[\sinh(\xi\sigma_p)] = \frac{\ln\dot{\varepsilon}}{n} + \frac{Q_{\text{act}}}{nRT} - \frac{\ln A_n}{n}. \tag{8}$$

Take logarithm on both sides of Eqs. (4) and (5) to obtain:

$$\ln\dot{\varepsilon} = \ln A_n + n_1 \ln\sigma_{\text{p}}, \tag{9}$$

$$\ln\dot{\varepsilon} = \ln A_n + \beta\sigma_{\text{p}}. \tag{10}$$

The value of β and n_1 is the slope of the $\ln\dot{\varepsilon} - \ln\sigma_p$ curve and $\ln\dot{\varepsilon} - \sigma_p$ curve. The two curves are obtained by linear fitting, as shown in Figs. 6 and 7.

$$\xi = \beta/n_1 = 0.002266. \tag{11}$$

Take logarithm on both sides of Eq. (3) to obtain:

$$Q_{\text{act}} = R\left(\frac{\partial\ln\dot{\varepsilon}}{\partial\ln[\sinh(\xi\sigma)]}\right)_T \left(\frac{\partial\ln[\sinh(\xi\sigma)]}{\partial(1/T)}\right)_{\dot{\varepsilon}}. \tag{12}$$

According to Eq. (12), there are two parts on the right side of Eq. (12). Two curves which show the relationship of $\ln\dot{\varepsilon} - \ln[\sinh(\xi\sigma)]$ and $\ln[\sinh(\xi\sigma)] - 1/T$ are drawn

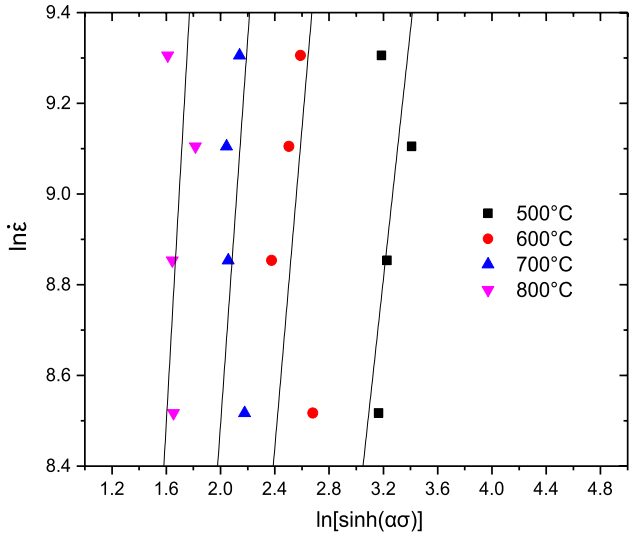

Fig. 8 $\ln \dot{\varepsilon} - \ln[\sinh(\xi\sigma)]$ curve

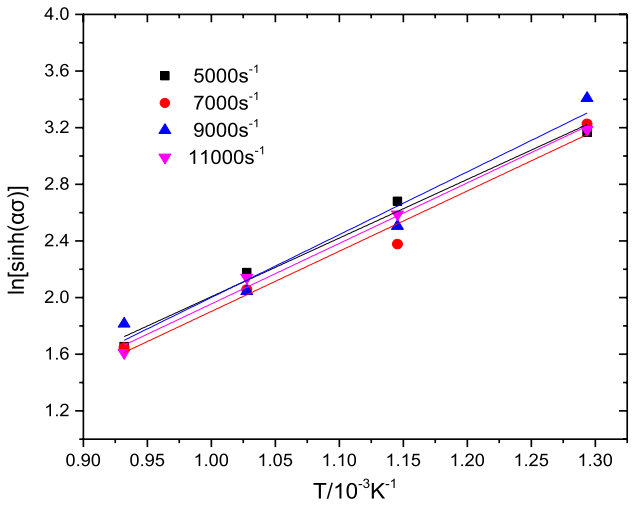

Fig. 9 $\ln[\sinh(\xi\sigma)] - \frac{1}{T}$ curve

respectively, as shown in Figs. 8 and 9. According to Figs. 8 and 9, we can get the following results:

$$\frac{\partial \ln \dot{\varepsilon}}{\partial \ln \sinh(\xi\sigma_p)} = n = 3.953, \tag{13}$$

$$\frac{\partial \ln \sinh(\xi\sigma_{\mathrm{p}})}{\partial(1/T)} = \frac{Q_{\mathrm{act}}}{nR} = 4.27. \tag{14}$$

Taking the above calculated values into Eq. (14), the deformation activation energy of Inconel 718 is calculated as follows:

$$Q_{\mathrm{act}} = 140334.46$$

The value of Q_{act} and the corresponding strain rate at different temperatures are brought into Eq. (6), and the Z value is obtained as follows:

$$Z = \dot{\varepsilon} \exp\left(\frac{140334.46}{RT}\right). \tag{15}$$

According to the curve which describe the relationship between $\ln Z$ and $\ln\left[\sinh(\xi\sigma_{\mathrm{p}})\right]$ (see Fig. 10), the slope can be calculated as 8.045, and $A_n = 29{,}000{,}000$.

The peak flow stress σ_{p} can be written as a function of Z, as shown in Eq. (16).

$$\sigma_{\mathrm{p}} = 441.306 \times \left\{ \left(\frac{Z}{2.9 \times 10^7}\right)^{0.12} + \left[\left(\frac{Z}{2.9 \times 10^7}\right)^{0.24} + 1 \right]^{0.5} \right\}. \tag{16}$$

Through the analysis of the experimental results (see Fig. 11), it is easy to find the relationship between the peak strain ε_{p} and Z value, as shown in Eq. (17).

$$\varepsilon_{\mathrm{p}} = 0.235 Z^{0.0146}. \tag{17}$$

Therefore, the critical strain for dynamic recrystallization can be expressed as follows.

$$\varepsilon_{\mathrm{c}} = 0.8\varepsilon_{\mathrm{p}} = 0.1888 Z^{0.0146}. \tag{18}$$

As long as the temperature and strain rate are given, the critical strain value of dynamic recrystallization can be obtained. It can be found from Eq. (18) that the lower the temperature, the higher the critical strain for dynamic

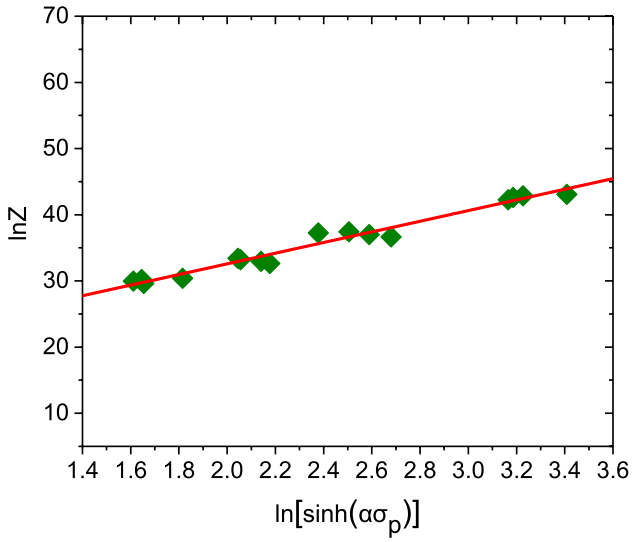

Fig. 10 $\ln Z$–$\ln\left[\sinh(\xi\sigma_{\mathrm{p}})\right]$ relationship diagram

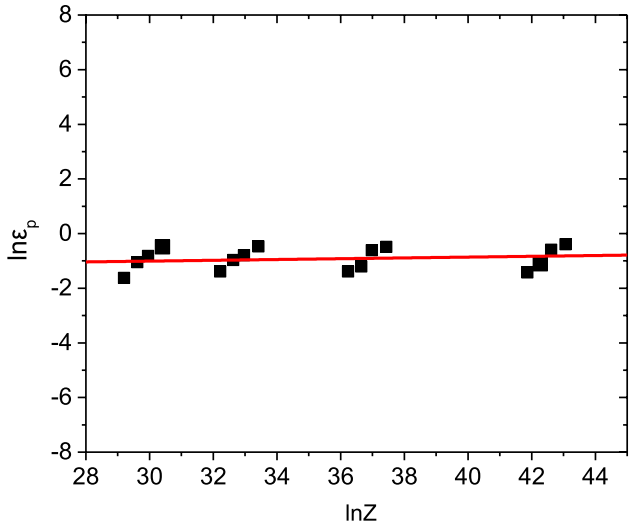

Fig. 11 $\ln\varepsilon_p$–ln$Z$ relationship diagram

recrystallization. This is because that there is stored energy for deformation in the process of deformation, and the higher the deformation storage energy contained in the microstructure at high temperature, the lower the deformation energy required for dynamic recrystallization. With the increase in strain rate, the critical strain of dynamic recrystallization will increase.

The value of S can be obtained by fitting the $\ln(\sigma/\sigma_p)$ –ln $\left[(\varepsilon/\varepsilon_p)\exp(1-\varepsilon/\varepsilon_p)\right]$ curve, as shown in Fig. 12. S is a straight line and these graphs show that the parameter S is a function of temperature. It can well describe the relationship with temperature, as shown in Eq. (19).

$$S = aT + b. \tag{19}$$

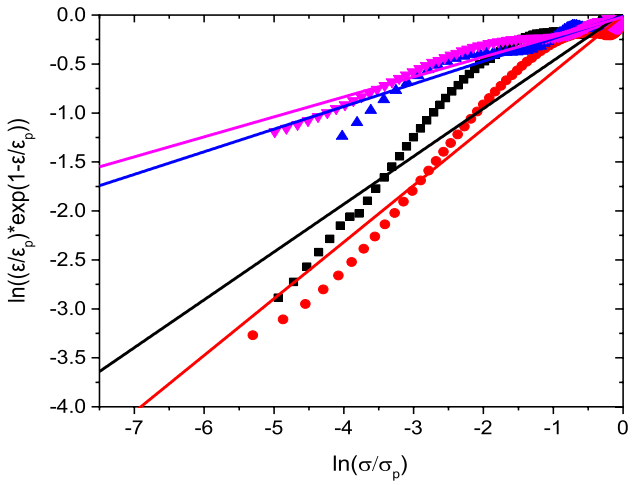

Fig. 12 Relationship diagram of $\ln(\sigma/\sigma_p)$–ln $\left[(\varepsilon/\varepsilon_p)\exp(1-\varepsilon/\varepsilon_p)\right]$

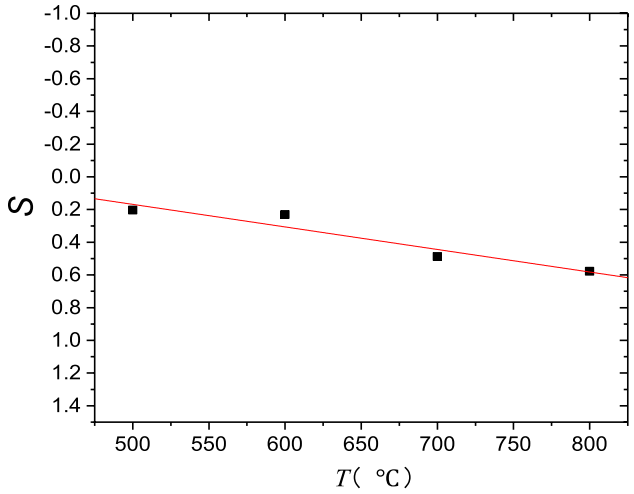

Fig. 13 Relationship diagram between S and T

In Eq. (9), the a and b are constants, which can be calculated by Fig. 13.

$$S = 0.0006T - 0.11. \tag{20}$$

Based on the above analysis, the dynamic behavior for work hardening of Inconel 718 at high temperature and high strain rate can be described as follow.

$$\begin{cases} \dfrac{\sigma}{\sigma_p} = \left[\dfrac{\varepsilon}{\varepsilon_p}\exp\left(1-\dfrac{\varepsilon}{\varepsilon_p}\right)\right]^S \\ \sigma_p = 441.306 \times \left\{\left(\dfrac{Z}{2.9\times10^7}\right)^{0.12} + \left[\left(\dfrac{Z}{2.9\times10^7}\right)^{0.24} + 1\right]^{0.5}\right\} \\ \varepsilon_c = 0.8\varepsilon_p = 0.1888Z^{0.0146} \\ Z = \dot{\varepsilon}\exp\left(\dfrac{140334.46}{RT}\right) \\ S = 0.0006T - 0.11. \end{cases}$$

The accuracy of the work hardening model is verified by comparing the experimental values with the predicted values, as shown in Fig. 14.

To verify the established constitutive model of flow stress, the predicted value is compared with the experimental value at high temperature and high strain rate, as shown in Fig. 15. The results show that the correlation coefficient between the predicted flow stress value and the experimental value is 0.94, and the relatively high relative coefficient verifies the accuracy of the established flow stress constitutive model.

3.3.2 Softening behavior

At present, the Avrami equation [15] is generally used to express the dynamic recrystallization volume fraction (X_{DRX}) in the process of thermal deformation.

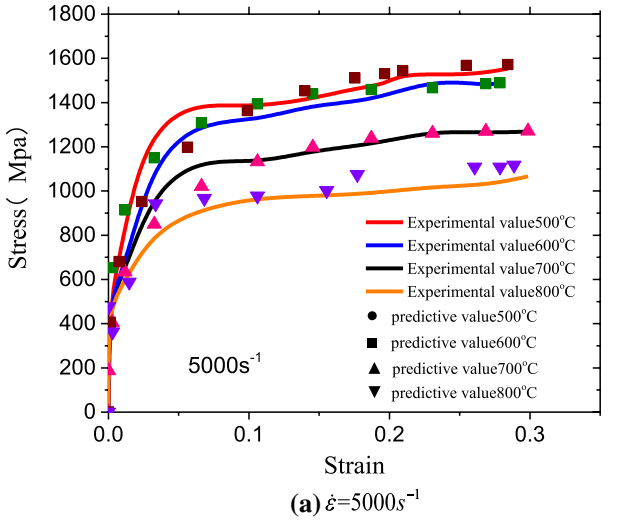

(a) $\dot{\varepsilon}$=5000s^{-1}

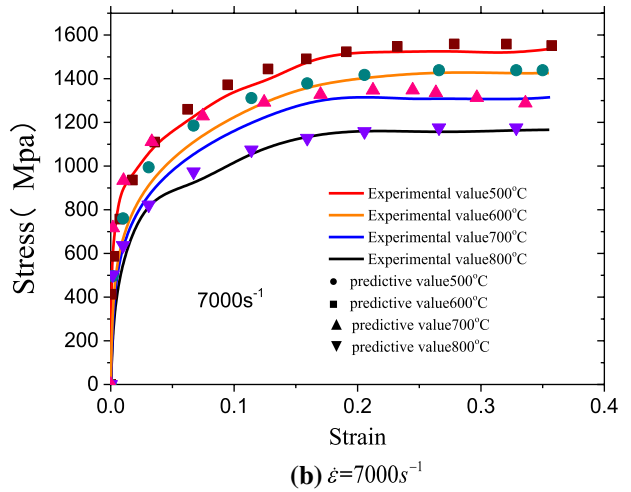

(b) $\dot{\varepsilon}$=7000s^{-1}

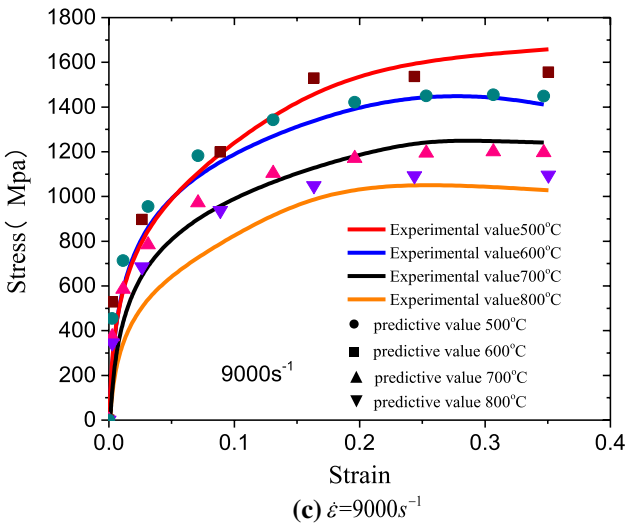

(c) $\dot{\varepsilon}$=9000s^{-1}

Fig. 14 Comparison between experimental value and predicted value of stress under different strain rates

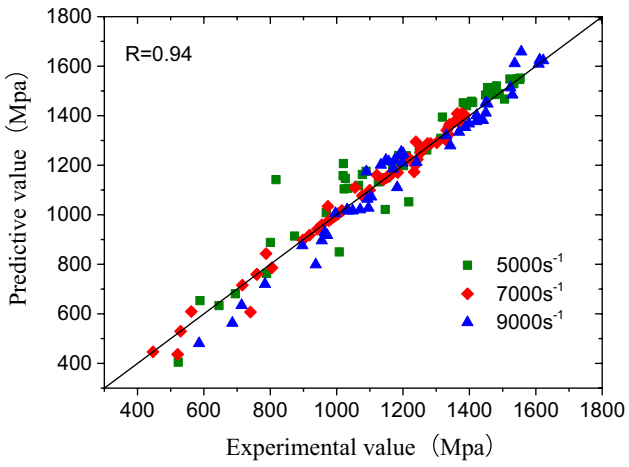

Fig. 15 Comparison between experimental values and predicted values of flow stress

$$X_{\mathrm{DRX}} = 1 - \exp\left[-K_{\mathrm{d}}\left(\frac{\varepsilon - \varepsilon_{\mathrm{c}}}{\varepsilon_{\mathrm{p}}}\right)^{n_{\mathrm{d}}}\right] (\varepsilon \geq \varepsilon_{\mathrm{c}}). \tag{21}$$

When the strain is greater than the critical strain, dynamic recrystallization usually occurs, especially at high temperature. In general, the material volume fraction of dynamic recrystallization during thermal deformation can be expressed as Eq. (22) [15].

$$X_{\mathrm{DRX}} = \frac{\sigma - \sigma_{\mathrm{p}}}{\sigma_{\mathrm{s}} - \sigma_{\mathrm{p}}}, \tag{22}$$

where ε_{p} is peak strain, ε_{c} is critical strain. K_{d} and n_{d} are parameters in dynamic recrystallization equation respectively, whose values can be calculated by regression analysis of formula (22) [15].

$$\ln[-\ln(1 - X_{\mathrm{D}})] = \ln K_{\mathrm{d}} + n_{\mathrm{d}} \ln\left(\frac{\varepsilon - \varepsilon_{\mathrm{c}}}{\varepsilon_{\mathrm{p}}}\right). \tag{23}$$

According to the experimental calculation, it is easy to obtain the values of K_{d} and n_{d}, and the average value of K_{d} is 4.28. The relationship between n_{d} with $\ln Z$ is shown in Fig. 16.

The dynamic recrystallization expression of Inconel 718 can be expressed as Eq. (24).

$$n_{\mathrm{d}} = 0.81325 - 0.0105 \ln Z. \tag{24}$$

Therefore, the dynamic recrystallization kinetic equation of Inconel 718 at high temperature and high strain rate is expressed as follows.

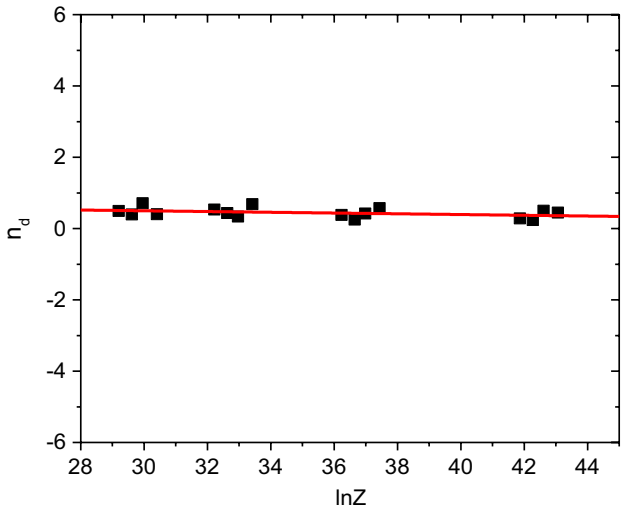

Fig. 16 Relationship diagram of $n_d - \ln Z$

$$\begin{cases} X_{DRX}=1-\exp\left[-K_d\left(\frac{\varepsilon-\varepsilon_c}{\varepsilon_p}\right)^{n_d}\right](\varepsilon \geq \varepsilon_c) \\ \varepsilon_p = 0.174Z^{0.0679} \\ \varepsilon_c = 0.8\ \varepsilon_p = 0.1393Z^{0.069} \\ n_d = 0.81325 - 0.0105\ln Z \\ K_d = 4.28. \end{cases} \quad (25)$$

3.4 Influence of dynamic behavior of material in cutting zone on cutting process

3.4.1 Effect of cutting deformation

Metallographic graph of chip root of Inconel 718 is shown in Fig. 17a. Figure 17b illustrates the metallographic graph of chip root of AISI1045 steel. Compared with the AISI1045 steel, inhomogeneous plastic deformation was observed in the metallographic graph of Inconel 718. It contains two areas: large deformation and non-deformation zone. According to Fig. 17a, it can be inferred that there are two deformation stages in cutting Inconel 718: compression deformation and shear deformation.

Because of the non-uniform strain and local large deformation in cutting Inconel 718, the deformation coefficient is larger than AISI1045 steel, as shown in Fig. 18.

Owing to the small heat transfer coefficient, the cutting temperature in tooltip is very high and the gradient of temperature distribution is large. Therefore, the yield strength σ_s of a material in the wedge layer in front of the cutting tool is reduced because of the high temperature. The cutting force appeared in the form of compressive stress σ_c. After receiving the compressive stress σ_c, the material in the wedge layer flowed along the tool rake face. The flow line of material and

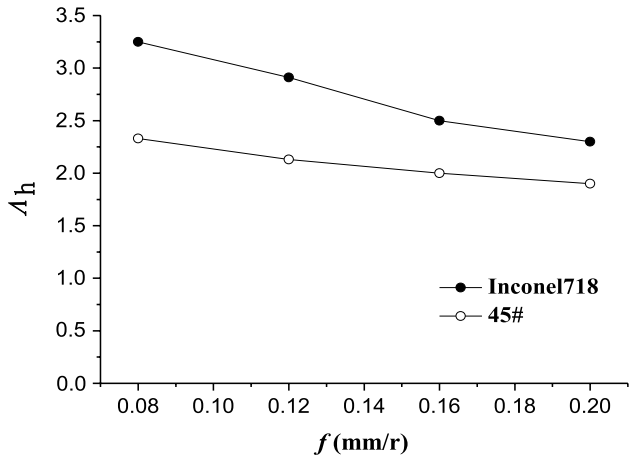

Fig. 18 Deformation coefficient of Inconel 718 and AISI1045

Fig. 17 Metallographic graph of chip root

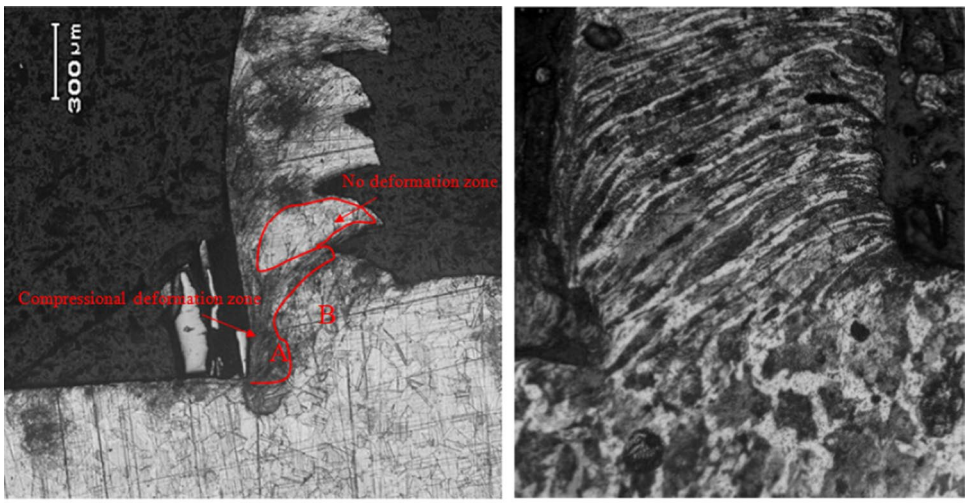

(a) Inconel718 **(b)** AISI1045 (Liu, 1985)

backflow phenomenon was observed clearly, as shown in Fig. 19. The stress, when the above phenomenon occurred, should meet the following requirement.

The normal stress distribution of the material AISI1045 is shown in Fig. 20. However, for Inconel 718, because of the extrusion-flow deformation of the material in the compressive stage, the distribution of normal stress has been changed. When σ_c increased to equal to σ_s ($\sigma_c = \sigma_s$), the cutting force appeared in the form of shear stress τ. The equilibrium position of shear stress for cutting layer material changed. The shear plane moved to the cutting layer inside. Therefore, there is a micro deformation zone between the extrusion zone and the shear zone, which promotes the formation of cutting segments, as shown in Fig. 21.

According to Fig. 21b which illustrates the stress distribution of Inconel 718, the cutting layer received compress force. In the light of the cutting principle that the angle between the direction of normal stress and the maximum shear stress is 45°, in cutting Inconel 718, the real shear angle is 45°. Therefore, between the areas which received normal stress and shear stress respectively, the undeformed zone occurred (shown in the shadow region in Fig. 22), which led to a non-uniform deformation of the chip.

According to Fig. 22, the shear angle ϕ has a relationship with the parameter l, which can be written as [6]:

$$\begin{aligned} \frac{h_D/\sin 45^\circ}{\sin\phi} &= \frac{l}{\sin(45^\circ-\phi)} \\ \frac{h_D/\sin 45^\circ}{\sin\phi} &= \frac{l}{\sin(45^\circ-\phi)} \\ \frac{h_D/\cos 45^\circ}{\sin\phi} &= \frac{l}{\sin 45^\circ\cos\phi-\cos 45^\circ\sin\phi} \\ tg\phi &= \frac{h_D}{l+h_D} < 1. \end{aligned} \tag{26}$$

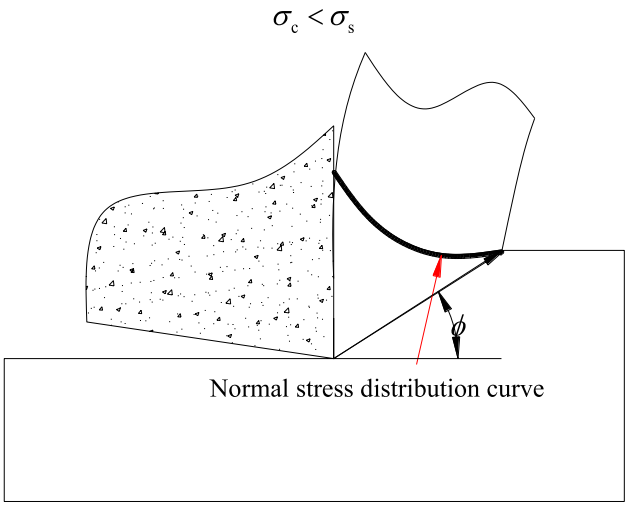

Fig. 20 Normal stress distribution of the material AISI1045 [28]

It can be seen from the above equations that the theoretical shear angle $\phi < 45^\circ$ in the process of machining Inconel 718.

Through cutting simulation analysis (using ABAQUS software, the material parameters are obtained from the stress–strain curve and the cutting speed $v_c = 90$ m/min), and according to the analysis results, the stress distribution diagram in the cutting area can be observed intuitively, as shown in Fig. 23. According to the analysis, the material in the cutting zone near the rake face bears the compressive stress, while the material near the free surface of the chip bears the tensile stress. The stress diagram of the shear band during the cutting deformation is shown in Fig. 23a. Therefore, under the condition of tensile stress on the free surface between the chip segment and the cutting layer material, cracks will occur along with the cutting process, resulting in stress concentration. The shear localization resulted in serrated cutting, which was consistent with the

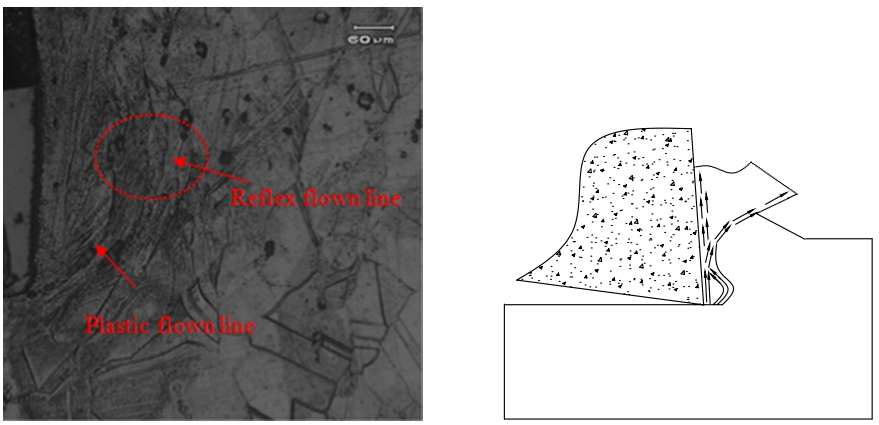

(a) Enlarged view of area A in Fig.16- a **(b)** Schematic diagram of back flow phenomenon

Fig. 19 Micrographs by SEM and schematic diagram of cutting deformation

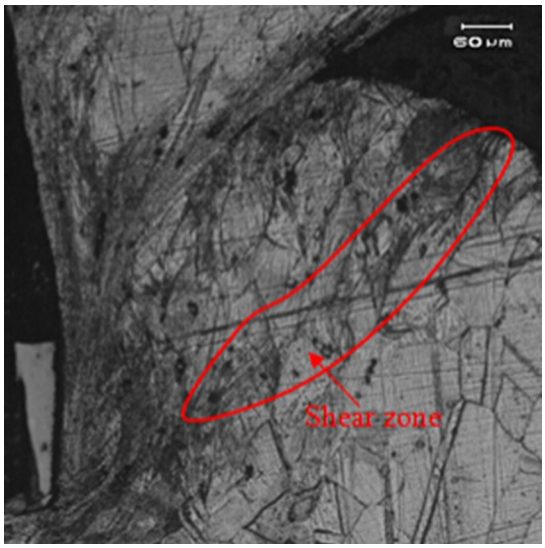

(a) Enlarged view of area B in Fig.16-a

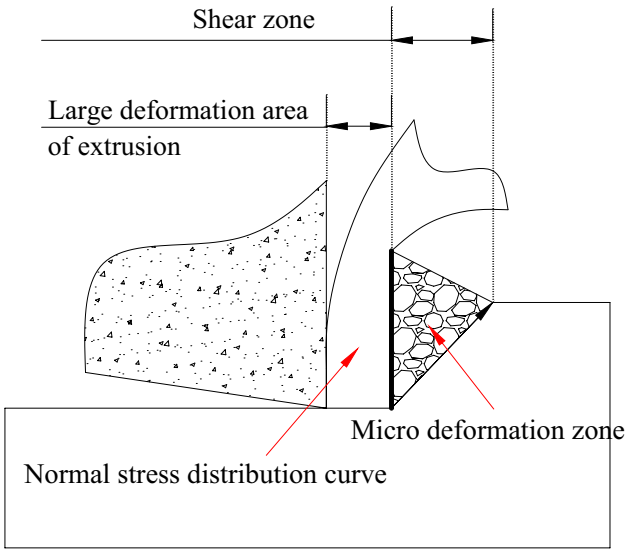

(b) Schematic diagram of stress distribution

Fig. 21 Micrographs by SEM of shear zone and schematic diagram of stress distribution

observation of the metallographic diagram of chip root, as shown in Fig. 23b.

According to the above analysis, the chip formation mechanism can be summarized as follows: high cutting temperature makes the material in the cutting zone soften (dynamic recrystallization) → the wedge-shaped cutting layer is extruded plastic deformation → the shear plane moves to the internal cutting layer → the shear surface and the extrusion deformation area form a micro deformation area → the cutting section forms a fast forming tensile stress → under the condition of tensile stress, crack occurs

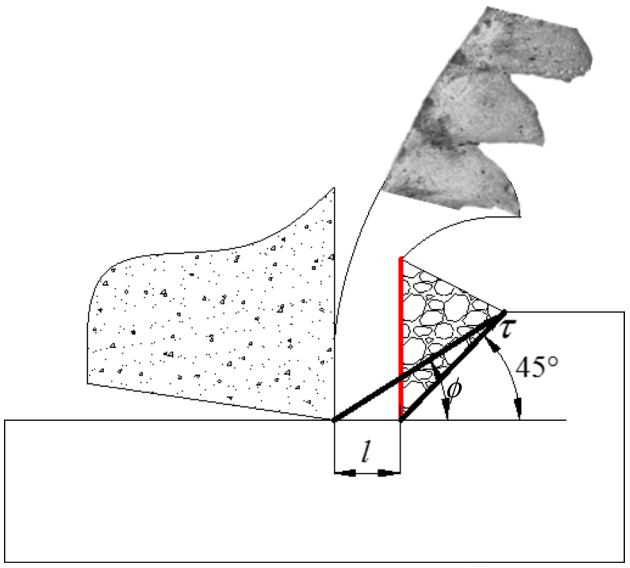

Fig. 22 Schematic diagram of stress distribution in cutting layer

in the free surface → stress concentration → the shear is localized and the chips are serrated.

The complex deformation of the material in a cutting zone not only led to the formation of a serrated chip but also the fluctuation of cutting force, thereby leading to alternative loads in the cutting process. The frequency of alternative load is the generation frequency of the serrated chip.

The frequency of alternative load can be expressed as [6]:

$$f_{\mathrm{X}} = \frac{v_{chip}}{L}. \tag{27}$$

The frequency of alternative load changed with the cutting speed, as shown in Fig. 24.

3.4.2 Chip side flow

The chip side flow was observed in the process of cutting Inconel 718. There are basically two types of chip side flow. One is irregular burrs and the other is a micro-ribbon chip, as shown in Fig. 25.

Owing to the tool nose radius and negative edge inclination angle, chip thickness gradually reduced to 0 at tooltip along the cutting edge, and the material at tooltip subjected to high compressive stress. Therefore, integrated above factors and the thermal softening behavior of the material, the material at tooltip squeezed out easily and led to the formation of the irregular burrs in the stage of plastic deformation, as shown in Fig. 26.

When wear occurred at tool tip, under the compressive stress, the materials would fill the wear valley and squeezed out along the chip edge. The micro-ribbon chip formed, as shown in Fig. 27.

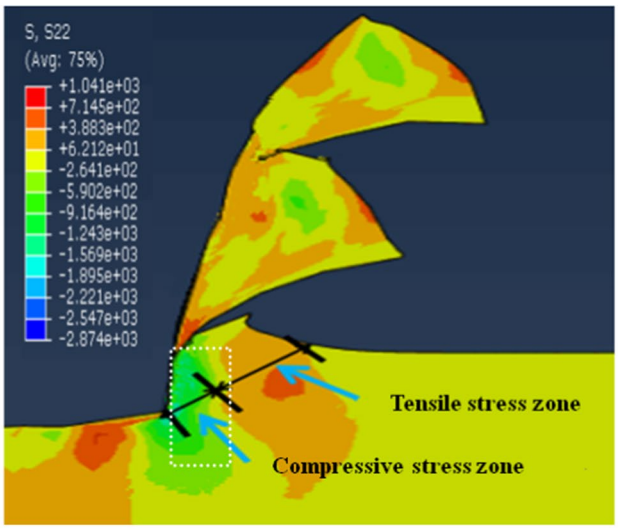

(a) Stress diagram of the shear band during the cutting deformation

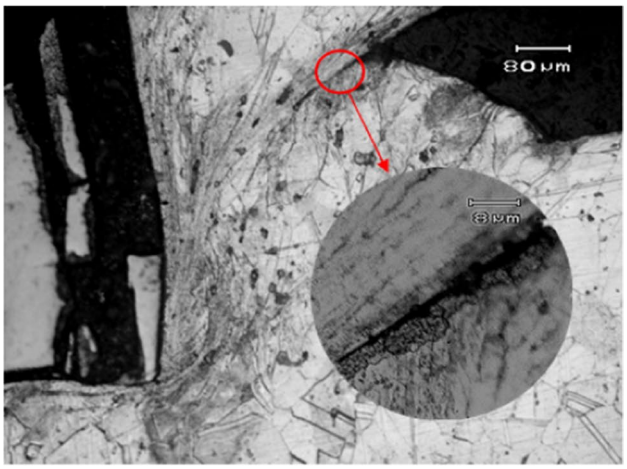

(b) Metallographic diagram of chip root

Fig. 23 Stress distribution of the shear band and metallographic diagram of chip root

3.4.3 Influence on tool wea

Since the cutting tool subjected to cyclic loads, the wear debris formed and fell away from the tool surface. At the same time, the plastic flow of the material in the tool rake face, it led to erosion wear, as shown in Fig. 28. Due to the hard particles and the randomness of wear debris generation, the erosion surface morphology generated is also diverse. It can be seen clearly that there were furrows, micro cutting and deformation lips, and so on in the tool rake face, as shown in Fig. 28b, c.

In high-speed cutting of Inconel 718, the Fe and Ni elements in the workpiece and the Co element in the tool substrate belong to the same family and have high affinity. Under the high temperature and high stress in the contact

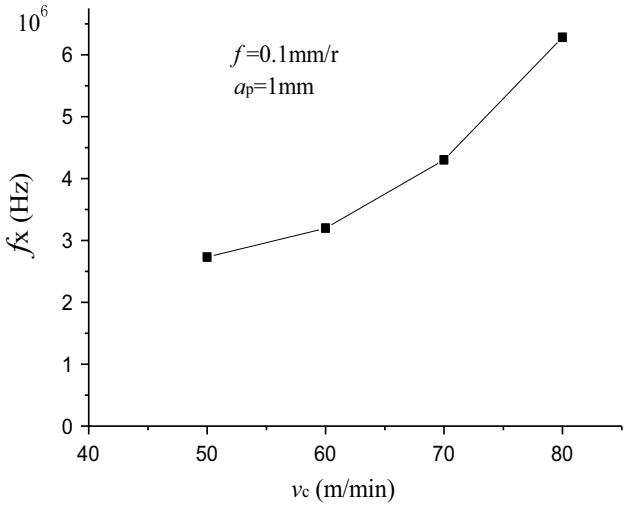

Fig. 24 Variation of f_x with cutting speed v_c

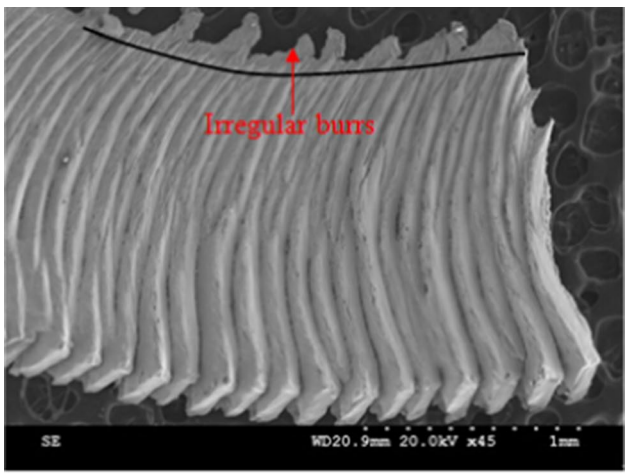

(a) Micrographs by SEM of irregular burrs of chip

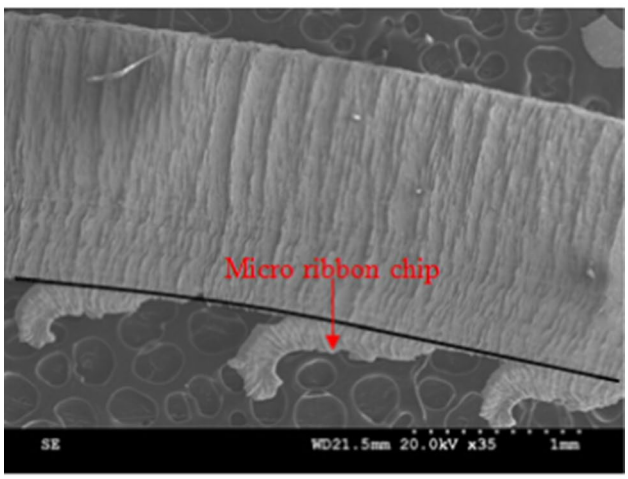

(b) Micrographs by SEM of micro-ribbon chip

Fig. 25 Micrographs by SEM of chip side flow

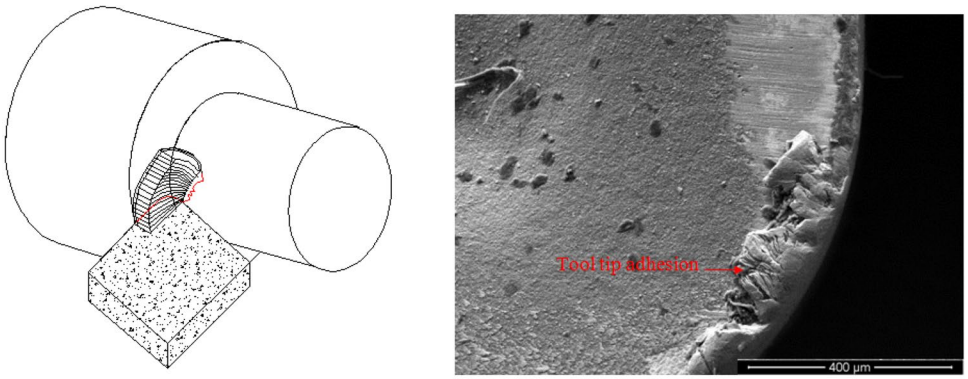

Fig. 26 Chip side flow (irregular burrs)

(a) Formation diagram of irregular burrs **(b)** Wear morphology of tool tip

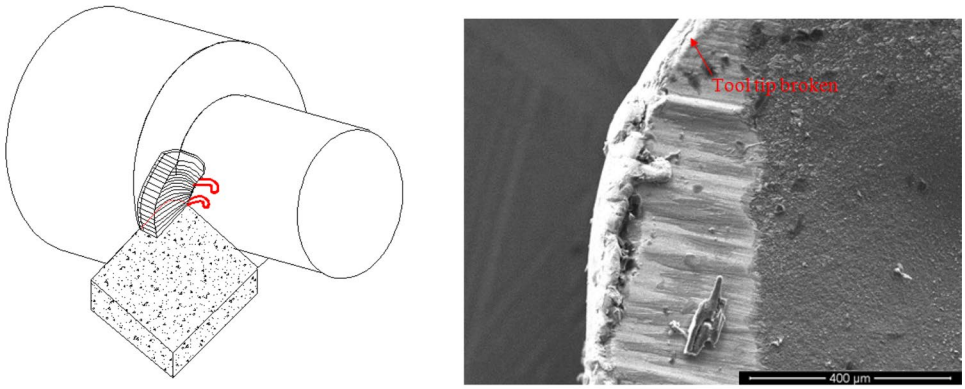

Fig. 27 Chip side flow (micro-ribbon chip)

(a) Formation diagram of micro-ribbon chip **(b)** Wear morphology of tool tip

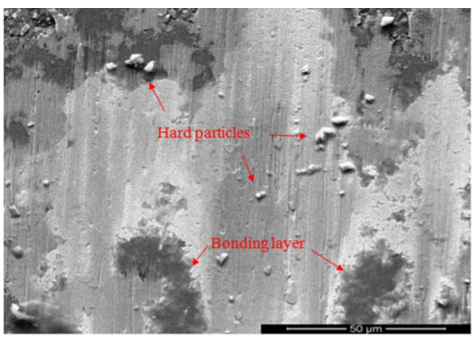

Fig. 28 Tool wear morphology

(a) Wear morphology of rake face

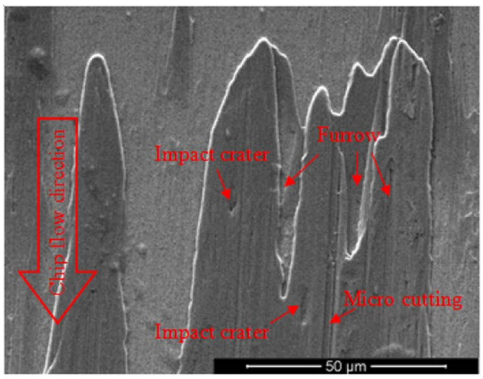

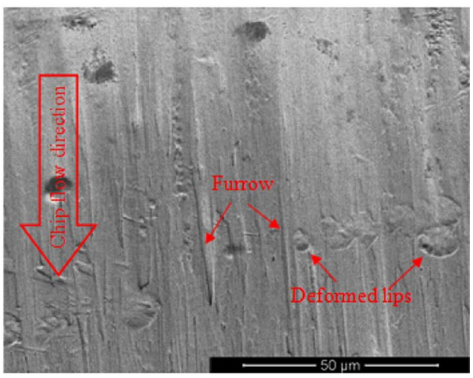

(b) Erosion surface morphology **(c)** Furrow and deformation lips

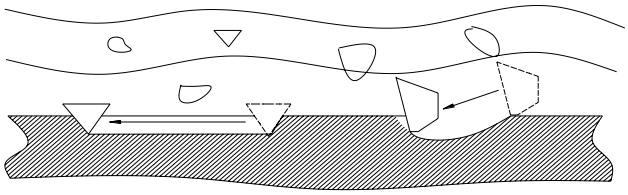

Fig. 29 Erosion wear mechanism model

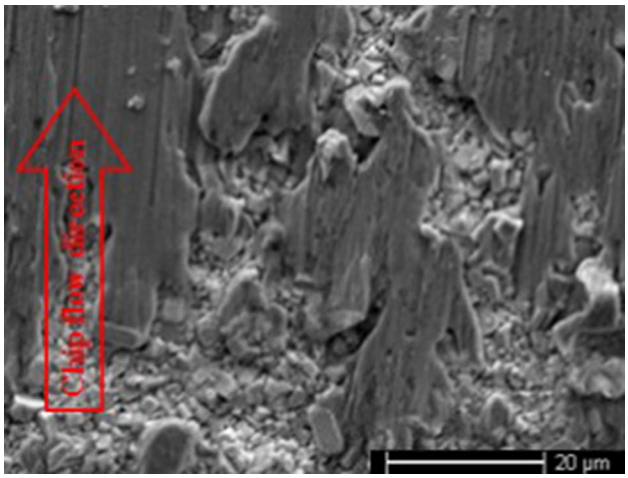

Fig. 30 Peeling off of tool materials

area, the Fe and Ni elements in the workpiece material and the Co element in the cutting tool diffused to the tool surface layer through the grain boundary [12]. The new generated material weakens the contact with the tool (WC, Tic, TaC), which can reduce the strength of the tool surface, and the hard particles in the plastic flow can impact the tool surface to cut out the pits, or the hard particles pressed into the cutting surface can plough to plow out the groove marks. The mechanism model is shown in Fig. 29.

In the case of material plastic flow in front of the tool, the workpiece material adheres to the tool rake face due to softening, forming a bonding layer. Its peeling will take away the tool material and form an exposed tool matrix. The wear morphology is shown in Fig. 30.

4 Conclusions

In this paper, the cutting experiments, explosive fast tool-drop tests and SHPB tests were carried out to study the plastic dynamic behavior of the materials in the cutting zone and its effects on the cutting process in machining Inconel 718. The conclusions can be drawn as:

(1) The constitutive model characterizing plastic behavior of Inconel 718 under high temperature and the high strain was established, which can better reflect the softening and hardening mechanism of the material during deformation. The main softening mechanism is dynamic recrystallization.
(2) The mechanism of non-uniform deformation and shear localization in the process of chip formation was revealed, which leads to the formation of sawtooth chips, and then caused the fluctuation of cutting force at a certain frequency. It made the tool surface bear the alternating load.
(3) When cutting Inconel 718 at high speed, due to the behavior of tool wear and material softening, the materials in the cutting area flow laterally under the action of tool extrusion, and there are two types: one is an irregular burr, and the other is micro-chip.
(4) In the cutting process, due to the special deformation form of the material in the cutting area, the tool surface leads to the erosion wear of the tool surface under the plastic flow of softened material and alternating load. Due to the randomness of the formation of hard particles and wear debris, the wear patterns of the formed erosion surface are also diverse.

Acknowledgements This research is supported by Science and Technology Planning project of Jilin Province (20210201043GX), Natural Science Foundation of Jilin Province (20200201064JC), Project of Science and Technology Bureau of Changchun City, Jilin Province (21ZY40), and Opening Project of the Key Laboratory of Advanced Manufacturing and Intelligent Technology (Ministry of Education), Harbin University of Science and Technology (KFKT202102).

Funding This research is supported by Science and Technology Planning Project of Jilin Province (20210201043GX), Natural Science Foundation of Jilin Province (20200201064JC), Project of Science and Technology Bureau of Changchun City, Jilin Province (21ZY40), and Opening Project of the Key Laboratory of Advanced Manufacturing and Intelligent Technology (Ministry of Education), Harbin University of Science and Technology (KFKT202102).

Declarations

Conflict of interest The authors declare no competing interests.

Ethical approval This article does not contain any studies with human participants or animals performed by any of the authors.

References

1. Cingara A, McQueen HJ. New formula for calculating flow curves from high temperature constitutive data for 300 austenitic steels. J Mater Process Tech. 1992;36:31–42. https://doi.org/10.1016/0924-0136(92)90236-L.

2. Costes JP, Guillet Y, Poulachon G, Dessoly M. Tool-life and wear mechanisms of CBN tools in machining of Inconel 718. Int J Mach Tool Manuf. 2007;7(7–8):1081–7. https://doi.org/10.1016/j.ijmachtools.2006.09.031.
3. Dvaies MA, Chou Y, Evsna CJ. On chip morphology, tool wear and cutting mechanics in finish hard turning. CIRP Ann Manuf Technol. 1996;45:77–82. https://doi.org/10.1016/S0007-8506(07)63020-0.
4. Dvaies MA, Buns TJ, Evnas CJ. On the dynamics of chip of formation in machining hard metals. CIRP Ann Manuf Technol. 1997;46:25–30. https://doi.org/10.1016/S0007-506(07)60768-9.
5. Elbestawi MA, Srivastava AK, El-Wardany TI. A model for chip formation during machining of hardened steel. CIRP Ann. 1996;8:71–6. https://doi.org/10.1016/S0007-8506(07)63019-4.
6. Gao D, Hao ZP, Han RD, et al. Study of cutting deformation in machining nickel-based alloy Inconel 718. Int J Mach Tools Manuf. 2011;51(6):520–7.
7. Hao ZP, Cui RR, Fan YH. Formation mechanism and characterization of shear band in high-speed cutting Inconel718. Int J Adv Manuf Techol. 2018;98:2791–9.
8. Jawahir IS, van Luttervlt CA. Recent developments in chip control research and applications. CIRP Ann Manuf Technol. 1993;42(2):659–93. https://doi.org/10.1016/S0007-8506(07)62531-1.
9. Komnaduri R, Schroeder T. On hear instability in machining nickel-iron base superalloy. J Eng For Ind. 1986;108:93–100. https://doi.org/10.1115/1.3187056.
10. Kouam J, Songmene V, Balazinski M, et al. Effects of Minimum Quantity Lubricating (MQL) conditions on machining of 7075–T6 aluminum alloy. Int J Adv Manuf Technol. 2015;79:1325–34. https://doi.org/10.1007/s00170-015-6940-6.
11. Kp A, Ms B, Hm C, et al. Influence of workpiece texture and strain hardening on chip formation during machining of Ti–6Al–4V alloy. Int J Mach Tool Manuf. 2022;173:103849. https://doi.org/10.1016/j.ijmachtools.2021.103849.
12. Liao YS, Shiue RH. Carbide tool wear mechanism in turning of Inconel 718 superalloy. Wear. 1996;193:16–24. https://doi.org/10.1016/0043-1648(95)06644-6.
13. Lin YC, Li KK, Li HB, et al. New constitutive model for high-temperature deformation behavior of Inconel 718 superalloy. Mater Design. 2015;74:108–18. https://doi.org/10.1016/j.matdes.2015.03.001.
14. Liu YC. Metal cutting principle. Shanghai: Shanghai Science and Technology Press; 1985. p. 19.
15. Lu BJ, Peng J, Shi DW, Tang AT, Pan FS. Constitutive modeling of dynamic recrystallization kinetics and processing maps of Mg−2.0Zn−0.3Zr alloy based on true stress−strain curves. Mater Sci Eng A. 2013;560:727–33. https://doi.org/10.1016/j.msea.2012.10.025.
16. Mahalle G, Kotkunde N, Gupta AK, et al. Microstructure characteristics and comparative analysis of constitutive models for flow stress prediction of inconel 718 alloy. J Mater Eng Perform. 2019;28:3320–31. https://doi.org/10.1007/s11665-019-04116-w.
17. Obikawa T, Usui E. Computational machining of titanium alloy-finite element modeling and a few results. J Manuf Sci Eng Transa ASME. 1996;118:208–15. https://doi.org/10.1115/1.2831013.
18. Recht RF. Catastrophic thermoplastic shear. J Appl Mech Trans ASME. 1964;86:189–93. https://doi.org/10.1115/1.3629585.
19. Recht RF. A dynamic analysis of high speed machining. J Eng For Ind. 1985;107:309–15. https://doi.org/10.1115/1.3186003.
20. Su GS, Liu ZQ, Li L, Wang B. Influences of chip serration on micro-topography of machined surface in high-speed cutting. Int J Mach Tool Manuf. 2015;89:202–7. https://doi.org/10.1016/j.ijmachtools.2014.10.012.
21. Shaw MC, Vyas A. The mechanism of chip formation with hard turning steel. CIRP Ann. 1998;47:77–83. https://doi.org/10.1016/S0007-8506(07)62789-9.
22. Sahraoui Z, Mehdi K, Jaber MB. Experimental study of the dynamic behavior of thin-walled tubular workpieces in turning cutting process. J Adv Manuf Syst. 2021;20(01):75–93. https://doi.org/10.1142/S0219686721500049.
23. Socha GM, Madejski B, Malicki M. Study on deformation-induced damage evolution for inconel718 superalloy with the use of innovative single-specimen method. J Theor App Mech. 2016;54:1379–90. https://doi.org/10.15632/jtam-pl.54.4.1379.
24. Sellars CM, Tegart WJ. The relationship between the resistance and the structural deformation in the hot. Mem Sci Rev Acta Metall Sin. 1966;64:731–46.
25. Thomas A, El-Wahabi M, Cabrera JM, et al. High temperature deformation of Inconel 718. J Mater Process Tech. 2006;177:469–72. https://doi.org/10.1016/j.jmatprotec.2006.04.072.
26. Wang B, Liu ZQ. Acoustic emission signal analysis during chip formation process in high speed machining of 7050–T7451 aluminum alloy and Inconel 718 superalloy. J Manuf Process. 2017;27:114–25. https://doi.org/10.1016/j.jmapro.2017.04.003.
27. Zener C, Hollomon JH. Effect of strain rate upon plastic flow of steel. J App Phys. 1944;15:22–32. https://doi.org/10.1063/1.1707363.
28. Zhou ZH. Metal cutting principle. Shanghai: Shanghai Science and Technology Press; 1993. p. 61.
29. Zbek O, Saruhan H. The effect of vibration and cutting zone temperature on surface roughness and tool wear in eco-friendly MQL turning of AISI D2. J Mater Res Technol. 2020. https://doi.org/10.1016/j.jmrt.2020.01.010.